Computers and Fluids 179 (2018) 67–77

Contents lists available at ScienceDirect

Computers and Fluids

journal homepage: www.elsevier.com/locate/compfluid

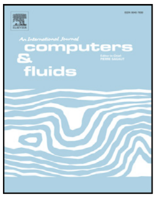

Benchmark solutions

An effective matrix-free implicit scheme for the magnetohydrodynamic solar wind simulations

Yuan Wang[a,b], Xueshang Feng[a,*], Changqing Xiang[a]

[a] SIGMA Weather Group, State Key Laboratory for Space Weather, National Space Science Center, Chinese Academy of Sciences, Beijing 100190, China
[b] College of Earth Sciences, University of Chinese Academy of Sciences, Beijing 100049, China

ARTICLE INFO

Article history:
Received 22 May 2018
Revised 7 September 2018
Accepted 9 October 2018
Available online 11 October 2018

MSC:
00-01
99-00

Keywords:
Magnetohydrodynamics
Solar wind
Finite volume
GMRES
LU-SGS

ABSTRACT

The magnetohydrodynamics (MHD) modeling of the steady solar wind is an essential and important ingredient in numerical space weather study. Numerically solving the MHD equation system is not an easy work due to its complexity by combining the Euler equations of gas dynamics with the Maxwells equations of electromagnetics and the solenoidal constraint. Moreover, the vast physical temporal and spatial scales of the solar wind simulation propose harsh requirements for computational efficiency and memory storage. Considering these factors, we develop an easily implemented finite volume (FV) scheme using the GMRES algorithm with an LU-SGS preconditioner for the three-dimensional (3D) MHD-based simulation. The steady-state solar wind from 1 R_s to 20 R_s during Carrington rotation (CR) 2051 is simulated for the validation of the proposed matrix-free implicit solver. Compared with the explicit solver, the implicit one can effectively enlarge the CFL number to 100 and achieve speedup ratios of 31.27 × and 28.05 ×, which reduces the computational time for the steady-state study from several days to only a few hours. The simulation captures main features of the solar corona and the mapped in-situ solar wind measurements. The scheme proposed here provides a promising choice to conduct the 3D MHD simulation of the solar wind background from the Sun to the Earth beyond.

1. Introduction

Numerical space weather modeling has been a promising tool used for space weather studies in recent decades, among which the study of steady solar wind is an essential and important ingredient. As the MHD equation system is the only self-consistent mathematical description currently used to model large-scale space weather phenomena, numerical MHD simulations are a powerful theoretical approach for retrieving the 3D structures and dynamics of the solar wind in solar-terrestrial space [1]. Mathematically, the ideal MHD equations are a hyperbolic partial differential equation (PDE) system by combining the Euler equations of gas dynamics with the Maxwell's equations of electromagnetics.

As solar-terrestrial physics phenomena involve vast physical temporal and spatial scales, efficiencies and computational costs in the numerical modeling of solar-terrestrial physics phenomena are important considerations in the numerical scheme. In an explicit time advance solver, the maximum allowable time step is always a much smaller value than that is needed to accurately resolve the transient behavior. The time step is set by the fast wave because the Courant–Friedrichs–Lewy (CFL) condition associated with the fast wave places much more restriction than that associated with the other waves [2]. However, an implicit scheme can remove the numerically imposed time-step constraint, allowing much larger time steps [3]. Generally at each time step or iteration, the implicit method need to solve a linear system of equations that is derived from the linearization of an implicit scheme. The most widely used methods to solve a linear system are iterative solution methods and approximate factorization methods [4]. Some efficient iterative solution methods have been developed for computational fluid dynamics (CFD), such as the generalized minimum residual (GMRES) with an incomplete lower-upper (iLU) factorization preconditioner. But the requirement of large memory to store the Jacobian matrix may prohibit themselves for large-scale problems. The lower-upper symmetric Gauss–Seidel (LU-SGS) method was first proposed by Jameson and Yoon [5] for the Euler equations. By making some approximations to the implicit operator, it can completely eliminate the storage of the matrix of the equation system in this approximate factorization method. Due to this attractive feature, LU-SGS has been successfully generalized and extended in many works. For example, Sitaraman et al. [6] applied this method to resistive MHD equations and developed a highly parallelizable matrix-free algo-

---

[*] Corresponding author.
E-mail addresses: wangyuan@spaceweather.ac.cn (Y. Wang), fengx@spaceweather.ac.cn (X. Feng), cqxiang@spaceweather.ac.cn (C. Xiang).

https://doi.org/10.1016/j.compfluid.2018.10.014
0045-7930/

rithm on unstructured grids with an analytic form of the convective flux Jacobian. However, when compared with the most efficient iterative methods such as GMRES with an iLU preconditioner, this method still converges slowly and is less effective. Luo et al. [4] gave a fast, matrix-free implicit method, i.e. a GMRES algorithm with an LU-SGS preconditioner, to solve Navier-Stokes equations, which combines the efficiency of the iterative methods with low memory requirement of approximate factorization methods in an effort.

Inspired by the above considerations, we develop an easily implemented finite volume (FV) scheme using the GMRES algorithm with an LU-SGS preconditioner for the MHD-based 3D simulation, which is an effective and matrix-free implicit time advance solver, to study the ambient solar wind for CR 2051. This FV scheme is based on the six-component mesh grid system proposed by Feng et al. [7], which consists of six identical component meshes to envelope a spherical surface with partial overlap on their boundaries. The paper is organized as follows. Section 2 presents a brief description of the model, including both the governing equations and the grid system. An easily implemented finite volume scheme goes into details in Section 3. Then follows the implicit time integration of the GMRES with an LU-SGS preconditioner in Section 4. In Section 5 numerical results of CR2051 are analyzed and compared with the observational results. Finally, conclusions are made in Section 6.

2. Model description

2.1. Governing equations

The solar wind evolution is governed by a modified ideal MHD equations, which is characterized with a solar wind source term $\mathbf{Q}_{\text{solar}}$. The dominance of the magnetic energy density in the solar corona may incur negative pressure in the course of the simulation. To mitigate this problem effectively, the split of the magnetic field $\mathbf{B}$ into a time-independent potential magnetic field $\mathbf{B_0}$ and a time-dependent deviation $\mathbf{B_1}$ (i.e. $\mathbf{B} = \mathbf{B_0} + \mathbf{B_1}$) is proposed in [7–9].

In numerical calculation, the solenoidal constraint $\nabla \cdot \mathbf{B} = 0$ can only be satisfied up to a discretization error, which will produce a force parallel to the magnetic field in the conservative form of the momentum equation causing unphysical effects [10] and result in failure. To solve this problem, we adopt the eight-wave formulation approach [11] by adding the powell source term $\mathbf{S}_{\text{powell}}$ to the right-hand-side of the governing equations to control $\nabla \cdot \mathbf{B_1}$. It introduces a divergence wave to advect the $\nabla \cdot \mathbf{B_1}$ errors away with the flow, which can control the $\nabla \cdot \mathbf{B_1}$ errors to the order of truncation error and eliminate the unphysical effects.

Then the governing equations can be written in brief as:

$$\partial_t \mathbf{U} + \nabla \cdot \mathbf{F} = \mathbf{S}_{\text{powell}} + \mathbf{Q}_{\text{solar}}, \tag{1}$$

with

$$\mathbf{U} = (\rho, \rho\mathbf{v}, \mathbf{B_1}, e_1)^T,$$

$$\mathbf{F} = \begin{pmatrix} \rho\mathbf{v} \\ \rho\mathbf{vv} + (p + \frac{\mathbf{B_1}\cdot\mathbf{B_1}}{2} + \mathbf{B_1}\cdot\mathbf{B_0})\mathbf{I} - \mathbf{B_1}\mathbf{B_1} - \mathbf{B_1}\mathbf{B_0} - \mathbf{B_0}\mathbf{B_0} \\ \mathbf{vB} - \mathbf{Bv} \\ \mathbf{v}(e_1 + p + \frac{\mathbf{B_1}\cdot\mathbf{B_1}}{2} + \mathbf{B_1}\cdot\mathbf{B_0}) - \mathbf{B}(\mathbf{v}\cdot\mathbf{B_1}) \end{pmatrix},$$

$$\mathbf{S}_{\text{powell}} = -\nabla \cdot \mathbf{B_1} \begin{pmatrix} 0 \\ \mathbf{B} \\ \mathbf{v} \\ \mathbf{v}\cdot\mathbf{B_1} \end{pmatrix}$$

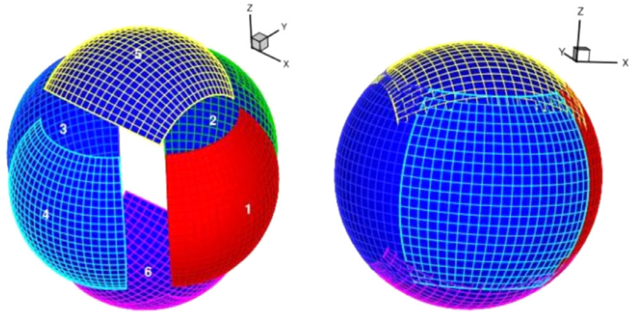

Fig. 1. The sketch of the six-component mesh grid system (left) and six identical components with partial overlap (right).

and

$$\mathbf{Q}_{\text{solar}} = \begin{pmatrix} 0 \\ \mathbf{j}_0 \times \mathbf{B}_0 + \rho[\mathbf{g} - \mathbf{\Omega} \times (\mathbf{\Omega} \times \mathbf{r})] - 2\rho\mathbf{\Omega} \times \mathbf{v} + \mathbf{S}_m \\ -\frac{\partial \mathbf{B}_0}{\partial t} \\ -\mathbf{B}_1 \cdot \frac{\partial \mathbf{B}_0}{\partial t} + \mathbf{E}\cdot\mathbf{j}_0 + \rho\mathbf{v}\cdot[\mathbf{g} - \mathbf{\Omega} \times (\mathbf{\Omega} \times \mathbf{r})] + Q_e + \mathbf{v}\cdot\mathbf{S}_m \end{pmatrix}.$$

Here, $\mathbf{U}$ is the conservative variables containing the mass density ρ, the momentum density $\rho\mathbf{v}$, the deviation magnetic field $\mathbf{B_1}$ and the modified total energy density $e_1 = \rho\frac{\mathbf{v}^2}{2} + \frac{p}{\gamma-1} + \frac{\mathbf{B_1}^2}{2}$. $\mathbf{F}$ is the flux term.

As for the solar source term $\mathbf{Q}_{\text{solar}}$, $\mathbf{r}$ is the position vector originating at the center of the Sun, and $\mathbf{g} = -GM/r^3 \cdot \mathbf{r}$ defines the solar gravitational force at $\mathbf{r}$. ρ, $\mathbf{v}$, p, $\mathbf{B}$, $\mathbf{r}$, t, and $\mathbf{g}$ are normalized by the characteristic values $\rho_S, a_0, \rho_S a_0^2, \sqrt{\rho_S a_0^2}, R_S, R_S/a_0$, and a_0^2/R_S, where ρ_S, a_0 and R_S are the mass density, sound speed on the solar surface and solar radius. $\mathbf{\Omega}$ is the angular speed of the solar rotation, with $|\mathbf{\Omega}| = 2\pi/25.38$ radian day^{-1} (here normalized by a_0/R_S) in the present study. γ is the ratio of specific heats, and according to Feng et al. [7] we set γ to vary from 1.05 to 1.5 along the heliocentric distance r, i.e. $\gamma = 1.05$ for $r/R_S \le 5$, $\gamma = 1.05 + 0.03(r/R_S - 5)$ for $5 < r/R_S \le 20$, and $\gamma = 1.5$ for $r/R_S > 20$. $\mathbf{E} = \mathbf{v} \times \mathbf{B}$ and $\mathbf{j}_0 = \nabla \times \mathbf{B}_0$. $\mathbf{S}_m$ and Q_e stand for the momentum source term and the volumetric heating function respectively, which are responsible for acceleration and heating of the solar wind. Taking into account the magnetic field topology effects [12], we prescribe them as

$$\mathbf{S}_m = M\left(\frac{r}{R_S} - 1\right)\exp\left(-\frac{r}{L_M}\right)\cdot\mathbf{r}/r,$$

$$Q_e = Q_1 \exp\left(-\frac{r}{L_{Q_1}}\right) + Q_2\left(\frac{r}{R_S} - 1\right)\exp\left(-\frac{r}{L_{Q_2}}\right).$$

Details about those parameters can be referred to Feng et al. [7].

2.2. Grid system

We inherit the six-component mesh grid system proposed by Feng et al. [7], that is composed of six identical component meshes to envelop a spherical surface with partial overlap on their boundaries. The sketch is shown in Fig. 1. This grid system provides a concise and balanced way to distribute computational domains to parallel computing system, and make it suitable to simulate large-scale heavy-calculation problems such as the solar wind evolution.

Each component grid is a low-latitude spherical mesh at $(\frac{\pi}{4} - \delta \le \theta \le \frac{3\pi}{4} + \delta) \cap (\frac{3\pi}{4} - \delta \le \phi \le \frac{5\pi}{4} + \delta)$, where δ is proportionally dependent on the grid spacing entailed for the minimum overlapping area. Each component is divided in the spherical coordinates with the same procedure. In the θ and ϕ directions, the par-

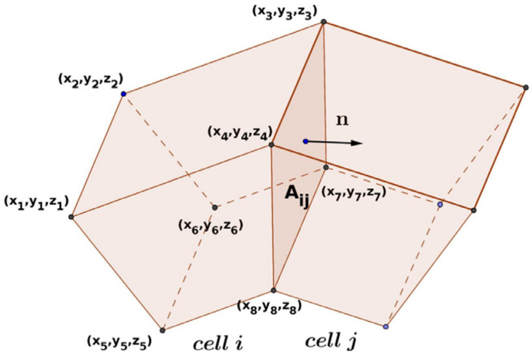

Fig. 2. The neighboring hexahedral cells i and j with the common face A_{ij}.

tition reads:

$$\begin{aligned} \theta_\jmath &= \theta_{\min} + \jmath\Delta\theta, & \jmath &= 0, 1, \cdots, N_\theta + 1 \\ \phi_\ell &= \phi_{\min} + \ell\Delta\phi, & \ell &= 0, 1, \cdots, N_\phi + 1 \end{aligned}$$

with $\Delta\theta = (\theta_{\max} - \theta_{\min})/(N_\theta - 1)$ and $\Delta\phi = (\phi_{\max} - \phi_{\min})/(N_\phi - 1)$. As for the mesh division in the radial direction, Feng et al. in [7] gave a suggestion for simulations of the solar wind as: for $1 - 25\mathrm{R_s}$ and $N_\phi = N_\theta = 2 \times 2^5 - 1$, $\Delta r(\imath) = 0.01\mathrm{R_s}$ if $r(\imath) < 1.1\mathrm{R_s}$; $\Delta r(\imath) = \min(A \times \log_{10}(r(\imath - 1)), \Delta\theta \times r(\imath - 1))$ with $A = 0.01/\log_{10}(1.09)$ if $r(\imath) < 3.5\mathrm{R_s}$; and $\Delta r(\imath) = \Delta\theta \times r(\imath - 1)$ if $r(\imath) \geq 3.5\mathrm{R_s}$. Parameters like 0.01, 1.09 etc. are chosen so as to make the cell as rectangular cube as possible, near the Sun. In this way, one mitigates this discrete or geometrical stiffness caused by disparate mesh cell widths. Field vectors on each component can be transformed to any other components in the Cartesian coordinate. This transformation can ensure data exchange between six components, especially when updating the boundary information after calculations at every time step. Details of vector transformation formulae are available in [7]. For the convenience of the later implicit treatment, we assign every cell in each component an identity number. For any cell $(\imath, \jmath, \ell)$ which is the $\imath$th cell in r direction, the $\jmath$th cell in θ direction and the ℓth cell in ϕ direction, we specify its identity number as $\jmath * (N_\theta + 2) * (N_\phi + 2) + \jmath * (N_\phi + 2) + \ell$. In the following statements, we will all use identity numbers to refer to cells. After the grid mesh partition in the spherical coordinates, we use their corresponding Cartesian ones to form the corresponding hexahedral cells as shown in Fig. 2.

In the following, a numerical implementation of the governing MHD equations on the hexahedral cells will be described in the Cartesian coordinate system, under the framework of MPI-parallel six-component mesh grid system.

3. Finite volume scheme

The finite volume form of Eq. (1) on the hexahedral cells in the six-component mesh grid system can be written as

$$\begin{aligned} &\Omega_i \frac{d\mathbf{U}_i}{dt} + \sum_{\mathrm{face}_j=1}^{6} \mathcal{R}^{-1}(\mathbf{n}_{ij})\mathbf{F}_x\Big(\mathcal{R}(\mathbf{n}_{ij})\mathbf{U}_{iL}, \mathcal{R}(\mathbf{n}_{ij})\mathbf{U}_{jR}\Big)A_{ij} \\ &\Omega_i\mathbf{S}_{\mathrm{powell}}(\mathbf{U}_i, (\nabla\cdot\mathbf{B_1})_i) + \Omega_i\mathbf{Q}_{\mathrm{solar}}(\mathbf{U}_i). \end{aligned} \tag{2}$$

The conservative variable $\mathbf{U}$ with subscript i refers to the calculated cell, whose identity number is i. And the subscript j stands for the identity number of cell i's neighbor cell. As shown in Fig. 2, cell i and cell j share a common interface, and we number it as face$_j$. Obviously, every cell i has six faces and six corresponding neighbor cells, and thus face$_j = 1, 2, \ldots, 6$. For the interface face$_j$ of cell i, its area is A_{ij} and its outward unit normal vector is $\mathbf{n}_{ij}$ pointing from cell i to cell j. Ω_i is the volume of cell i.

$\mathbf{F}_x$ stands for the numerical flux function in the x direction. $\mathbf{U}_{iL}$ is the value at the centroid of the interface ij extrapolated from cell i by reconstruction, while $\mathbf{U}_{jR}$ is that from cell j. $\mathcal{R}$ is the rotation matrix [13,14] that rotates the x-axis to the direction of $\mathbf{n}_{ij}$ and $\mathcal{R}^{-1}$ rotates it back. By utilizing rotation matrix, we can consider flux calculations only in the x direction about $\mathbf{F}_x$ and solve the equations in a brief and easily implemented way. The flux term of $\mathbf{F}_x$ at interface ij is the approximate Riemann problem, of which a variaty of solvers have been developed during the past dacades. For simplicity, Lax-Friedrichs method is applied for the presentation

$$\begin{aligned} \mathbf{F}_x\Big(\mathcal{R}(\mathbf{n}_{ij})\mathbf{U}_{iL}, \mathcal{R}(\mathbf{n}_{ij})\mathbf{U}_{jR}\Big) &= \frac{1}{2}\Big[\mathbf{F}_x\Big(\mathcal{R}(\mathbf{n}_{ij})\mathbf{U}_{iL}\Big) + \mathbf{F}_x\Big(\mathcal{R}(\mathbf{n}_{ij})\mathbf{U}_{jR}\Big)\Big] \\ &\quad - \frac{1}{2}|\lambda_{ij}|\Big(\mathcal{R}(\mathbf{n}_{ij})\mathbf{U}_{jR} - \mathcal{R}(\mathbf{n}_{ij})\mathbf{U}_{iL}\Big). \end{aligned} \tag{3}$$

where λ_{ij} is the largest eigenvalue of the Jacobian in the normal direction, taking its value at the interface of cell i and cell j, i.e.

$$\lambda_{ij} = |\mathbf{v}_{ij}\cdot\mathbf{n}_{ij}| + \sqrt{\frac{1}{2}\left(\frac{\gamma p_{ij} + \mathbf{B}_{ij}^2}{\rho_{ij}} + \sqrt{\left(\frac{\gamma p_{ij} + \mathbf{B}_{ij}^2}{\rho_{ij}}\right)^2 - 4\frac{\gamma p_{ij}B_{nij}^2}{\rho_{ij}^2}}\right)} \tag{4}$$

The subscript ij in Eq. (4) represents the corresponding arithmetic average values of $\mathbf{U}_{iL}$ and $\mathbf{U}_{jR}$.

The volume-averaged value of source terms $\mathbf{S}_{\mathrm{powell}}$ and $\mathbf{Q}_{\mathrm{solar}}$ is considered as follows. For instance, the volume-averaged value of $\mathbf{S}_{\mathrm{powell}}$ in cell I can be expressed by

$$\mathbf{S}_{\mathrm{powell}} = -(\nabla\cdot\mathbf{B_1})_i \begin{pmatrix} 0 \\ \mathbf{B}_i \\ \mathbf{v}_i \\ \mathbf{v}_i\cdot\mathbf{B}_{1_i} \end{pmatrix}$$

with

$$(\nabla\cdot\mathbf{B_1})_i = \frac{1}{\Omega_i}\sum_{\mathrm{face}_j=1}^{6}(\mathbf{B}_{1_{ij}}\cdot\mathbf{n}_{ij})A_{ij}, \mathbf{B}_{1_{ij}} = \frac{(\mathbf{B}_{1_{iL}} + \mathbf{B}_{1_{jR}})}{2}$$

Obviously, the volume-averaged value $\mathbf{S}_{\mathrm{powell}}$ is still a function of $\mathbf{U}_i$ and $\mathbf{U}_j$. For convenience, we denote it as $\mathbf{S}_{\mathrm{powell}}(\mathbf{U}_i, (\nabla\cdot\mathbf{B_1})_i)$.

3.1. Reconstruction

For the purpose of achieving second spatial accuracy, the limited linear least squares reconstruction is employed in this scheme, which has been successfully applied in many studies [11,15,16]. Denote $W_i^{(k)}$ the kth component of the primitive vector $\mathbf{W} = (\rho, \mathbf{v}, \mathbf{B}_1, p)^T$ at $\vec{\mathbf{x}}_i$, and $\nabla W^{(k)}$ its gradient at $\vec{\mathbf{x}}_i$. The general formula for the limited reconstruction is applied on the primitive variables on cell i

$$W_i^{(k)}(\vec{\mathbf{x}}_r) = W_i^{(k)} + \phi_i^{(k)}\nabla W_i^{(k)}\cdot(\vec{\mathbf{x}}_r - \vec{\mathbf{x}}_i). \tag{5}$$

where $\vec{\mathbf{x}}_i = (x_i, y_i, z_i)$ is the position of cell i's centroid, and $W_i^{(k)}(\vec{\mathbf{x}}_r)$ is the value to be reconstructed at $\vec{\mathbf{x}}_r$. Here we take $\vec{\mathbf{x}}_r$ as the face centroid of cell i.

As usual, the gradient $\nabla W^{(k)}$ at $\vec{\mathbf{x}}_r$ is evaluated by the least-square method [11]:

$$[\mathbf{L_1} \;\; \mathbf{L_2} \;\; \mathbf{L_3}]\cdot\nabla W_i^{(k)} = \mathcal{D}_w,$$

with

$$\mathbf{L_1} = \begin{pmatrix} \omega_{ng1}(x_{ng1} - x_i) \\ \vdots \\ \omega_{ngN}(x_{ngN} - x_i) \end{pmatrix}, \mathbf{L_2} = \begin{pmatrix} \omega_{ng1}(y_{ng1} - y_i) \\ \vdots \\ \omega_{ngN}(y_{ngN} - y_i) \end{pmatrix},$$

$$\mathbf{L_3} = \begin{pmatrix} \omega_{ng1}(z_{ng1} - z_i) \\ \vdots \\ \omega_{ngN}(z_{ngN} - z_i) \end{pmatrix}, \mathcal{D}_W = \begin{pmatrix} \omega_{ng1}(W_{ng1}^{(k)} - W_i^{(k)}) \\ \vdots \\ \omega_{ngN}(W_{ngN}^{(k)} - W_i^{(k)}) \end{pmatrix}.$$

The subscripts $ng1 \cdots ngN$ refer to the neighboring cells of cell i's vertices, and $N = 26$ for our hexahedral cell. $\omega_{ng} = \frac{1}{|\vec{\mathbf{x}}_{ng} - \vec{\mathbf{x}}_i|}$ is the weighting coefficient.

In Eq. (5), $\phi_i^{(k)}$ is the slope limiter. In the present paper, we use Venkatakrishnan limiter [17], which is believed to not only produce monotonic solution without oscillation, but also keep the accuracy and convergence. As usual, Venkatakrishnan limiter $\phi_{i,r}^{(k)}$ can be described as

$$\phi_{i,r}^{(k)} = \begin{cases} \psi\left(\frac{W_{i,\max}^{(k)} - W_i^{(k)}}{\nabla W_i^{(k)} \cdot (\vec{\mathbf{x}}_r - \vec{\mathbf{x}}_i)}\right) & \text{if } \nabla W_i^{(k)} \cdot (\vec{\mathbf{x}}_r - \vec{\mathbf{x}}_i) > 0 \\ \psi\left(\frac{W_{i,\min}^{(k)} - W_i^{(k)}}{\nabla W_i^{(k)} \cdot (\vec{\mathbf{x}}_r - \vec{\mathbf{x}}_i)}\right) & \text{if } \nabla W_i^{(k)} \cdot (\vec{\mathbf{x}}_r - \vec{\mathbf{x}}_i) < 0 \cdot \\ 1 & \text{if } \nabla W_i^{(k)} \cdot (\vec{\mathbf{x}}_r - \vec{\mathbf{x}}_i) = 0 \end{cases}$$

$W_{i,\max}^{(k)} = \max\left(W_i^{(k)}, W_{ng1}^{(k)}, \cdots W_{ngN}^{(k)}\right)$ and $W_{i,\min}^{(k)} = \min\left(W_i^{(k)}, W_{ng1}^{(k)}, \cdots W_{ngN}^{(k)}\right)$ are the maximum and minimum cell average values among cells $ng1 \cdots ngN$ and i. $\psi\left(\frac{\Delta_+}{\Delta_-}\right)$ is defined by the following function

$$\psi\left(\frac{\Delta_+}{\Delta_-}\right) = \frac{1}{\Delta_-}\left[\frac{\left(\Delta_+^2 + \epsilon^2\right)\Delta_- + 2\Delta_-^2\Delta_+}{\Delta_+^2 + \Delta_-\Delta_+ + 2\Delta_-^2 + \epsilon^2}\right],$$

with Δ_- represents the denominator of the function variable, and Δ_+ the numerator. $\epsilon^2 = (\mathcal{K}\Delta h)^3$, in which Δh is the local grid size or characteristic length of the cell V_i, and $\mathcal{K}$ is a tunable positive constant. In the present paper, according to [17], $\mathcal{K} = 0.3$ and Δh is taken to be the diameter of the inscribed circle within the cell. To prevent division by a very small value, Δ_- in the term $\frac{1}{\Delta_-}$ is replaced by $\text{sign}(\Delta_-)(|\Delta_-| + \omega)$ with $\omega = 10^{-12}$ in practical implementation. Finally, Venkatakrishnan limiter $\phi_i^{(k)}$ is defined by $\phi_i^{(k)} = \min\left(\phi_{i,r_1}^{(k)}, \cdots, \phi_{i,r_6}^{(k)}\right)$.

4. Implicit time integration

We rewrite Eq. (2) in a concise form as

$$\Omega_i \frac{d\mathbf{U}_i}{dt} = \mathbf{R}_i, \tag{6}$$

with

$$\mathbf{R}_i = \mathcal{F}_x(\mathbf{U}_i, \mathbf{U}_j) + \Omega_i \mathbf{S}_{\text{powell}}(\mathbf{U}_i, (\nabla \cdot \mathbf{B_1})_i) + \Omega_i \mathbf{Q}_{\text{solar}}(\mathbf{U}_i), \tag{7}$$

where

$$\mathcal{F}_x(\mathbf{U}_i, \mathbf{U}_j) \equiv \left\{ -\sum_{\text{face}_j=1}^{6} \mathcal{R}^{-1}(\mathbf{n}_{ij}) \mathbf{F}_x\left(\mathcal{R}(\mathbf{n}_{ij})\mathbf{U}_{iL}, \mathcal{R}(\mathbf{n}_{ij})\mathbf{U}_{jR}\right) A_{ij} \right\}.$$

The braced part is denoted by the function $\mathcal{F}_x(\mathbf{U}_i, \mathbf{U}_j)$ for the convenience of the later statement.

In order to obtain a steady-state solution, Eq. (6) is integrated in time with backward Euler method as

$$\Omega_i \frac{\Delta \mathbf{U}_i^n}{\Delta t} = \mathbf{R}_i^{n+1} \tag{8}$$

with $\Delta \mathbf{U}_i^n = \mathbf{U}_i^{n+1} - \mathbf{U}_i^n$ is the difference of conserved variables between time levels n and $n+1$, Δt is the time increment, and $\mathbf{R}_i$ is the right-hand side residual and is equal to zero for a steady-state solution. Linearizing the right-hand side of Eq. (8) in time we know that

$$\Omega_i \frac{\Delta \mathbf{U}_i^n}{\Delta t} = \mathbf{R}_i^n + \frac{\partial \mathbf{R}_i^n}{\partial \mathbf{U}} \Delta \mathbf{U}_i^n,$$

which can be then written in the following compact matrix form

$$\mathbf{A}\Delta\mathbf{U}^n = \mathbf{R}^n, \tag{9}$$

with $\mathbf{A} = \frac{\Omega}{\Delta t}\mathbf{I} - \frac{\partial \mathbf{R}^n}{\partial \mathbf{U}}$. This linear algebraic equations needs to be solved simultaneously at each time step. With respect to $\frac{\partial \mathbf{R}}{\partial \mathbf{U}}$ in cell i, from Eq. (7) we can get

$$\frac{\partial \mathbf{R}_i}{\partial \mathbf{U}_i} = \frac{\partial \mathcal{F}_x(\mathbf{U}_i, \mathbf{U}_j)}{\partial \mathbf{U}_i} + \Omega_i \frac{\partial \mathbf{S}_{\text{powell}}(\mathbf{U}_i, (\nabla \cdot \mathbf{B_1})_i)}{\partial \mathbf{U}_i} + \Omega_i \frac{\partial \mathbf{Q}_{\text{solar}}(\mathbf{U}_i)}{\partial \mathbf{U}_i}, \tag{10}$$

and

$$\frac{\partial \mathbf{R}_i}{\partial \mathbf{U}_j} = \frac{\partial \mathcal{F}_x(\mathbf{U}_i, \mathbf{U}_j)}{\partial \mathbf{U}_j}. \tag{11}$$

Here, the subscript j refers to cell i's corresponding neighbor cell.

To be specific, $\frac{\partial \mathcal{F}_x(\mathbf{U}_i, \mathbf{U}_j)}{\partial \mathbf{U}_i}$ in Eq. (10) is

$$\frac{\partial \mathcal{F}_x(\mathbf{U}_i, \mathbf{U}_j)}{\partial \mathbf{U}_i} = -\frac{1}{2}\left\{ \sum_{\text{face}_j=1}^{6} \mathcal{R}^{-1}(\mathbf{n}_{ij}) \left[\frac{\partial \mathbf{F}_x\left(\mathcal{R}(\mathbf{n}_{ij})\mathbf{U}_{iL}\right)}{\partial \mathbf{U}_i} + |\lambda_{ij}|\mathbf{I} \right] A_{ij} \right\},$$

and $\frac{\partial \mathcal{F}_x(\mathbf{U}_i, \mathbf{U}_j)}{\partial \mathbf{U}_j}$ in Eq. (11) is

$$\frac{\partial \mathcal{F}_x(\mathbf{U}_i, \mathbf{U}_j)}{\partial \mathbf{U}_j} = -\frac{1}{2}\mathcal{R}^{-1}(\mathbf{n}_{ij}) \left[\frac{\partial \mathbf{F}_x\left(\mathcal{R}(\mathbf{n}_{ij})\mathbf{U}_{jR}\right)}{\partial \mathbf{U}_j} - |\lambda_{ij}|\mathbf{I} \right] A_{ij}.$$

It should be noticed here that, λ_{ij} and $(\nabla \cdot \mathbf{B_1})_i$ are functions of the conservative variables about cells i and j, and should also be differentiated to obtain the Jacobian matrices of $\mathcal{F}_x(\mathbf{U}_i, \mathbf{U}_j)$ and $\mathbf{S}_{\text{powell}}(\mathbf{U}_i, (\nabla \cdot \mathbf{B_1})_i)$ respectively. However, taking true Jacobians is too complex and expensive. Barth in [18] analyzed the asymptotic convergence rates of both the true and the eigenvector transformed approximate Jacobian matrices. Test cases in his work showed that the spectral radius of the approximate Jacobian matrix was nearly identical with the true one at low CFL numbers, and was somewhat bigger at high CFL numbers. The performance of the approximate Jacobian matrix was mildly degraded at high CFL numbers but was still quite good overall, indicating that the use of eigenvector transformed approximate Jacobian is especially attractive to construct efficient, accurate implicit methods. And then, approximate Jacobians were widely adopted in many works [4,6,19]. Following previous experiments, we assume that λ_{ij} and $(\nabla \cdot \mathbf{B_1})_i$ are locally constant. Even with general degradation in convergence, it will take less CPU time to compute the Jacobian matrix, and the conditioning of the simplified Jacobian matrix can be improved [4,18], resulting in the reduction of computational cost to solve the resulting linear system. Virtually, the mismatch and inconsistency between the right- and left-hand sides of Eq. (9), which is caused by these approximations, do not affect the solution accuracy, for the steady-state solution to $\mathbf{R}(\mathbf{U}) = 0$ in Eq. (9) is looked for. This approximation works reasonably well for the small change in solution. As pointed out formerly [18,19], alternative choice may be the finite difference perturbation for Jacobian calculation.

4.1. LU-SGS Preconditioner

The LU-SGS method proposed in [5] shows good stability and competitive computational cost in comparison to explicit methods. The matrix $\mathbf{A}$ is split into a strict lower matrix $\mathcal{L}$, a diagonal matrix $\mathcal{D}$, and a strict upper matrix $\mathcal{U}$, i.e. $\mathbf{A} = \mathcal{D} + \mathcal{L} + \mathcal{U}$. Then Eq. (9) can be written as

$$(\mathcal{D} + \mathcal{L})\mathcal{D}^{-1}(\mathcal{D} + \mathcal{U})\Delta\mathbf{U} = \mathbf{R} + (\mathcal{L}\mathcal{D}^{-1}\mathcal{U})\Delta\mathbf{U}, \tag{12}$$

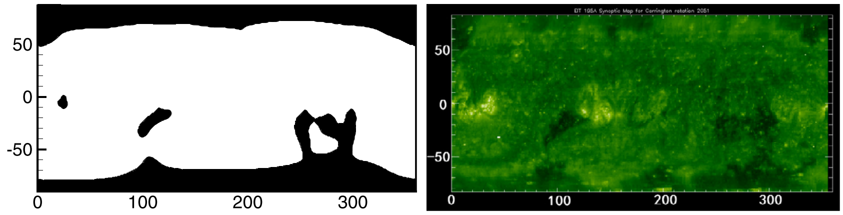

Fig. 3. Solar coronal holes near the solar surface simulated by the MHD model (left) and observed by the EIT/SOHO (right) for CR 2051.

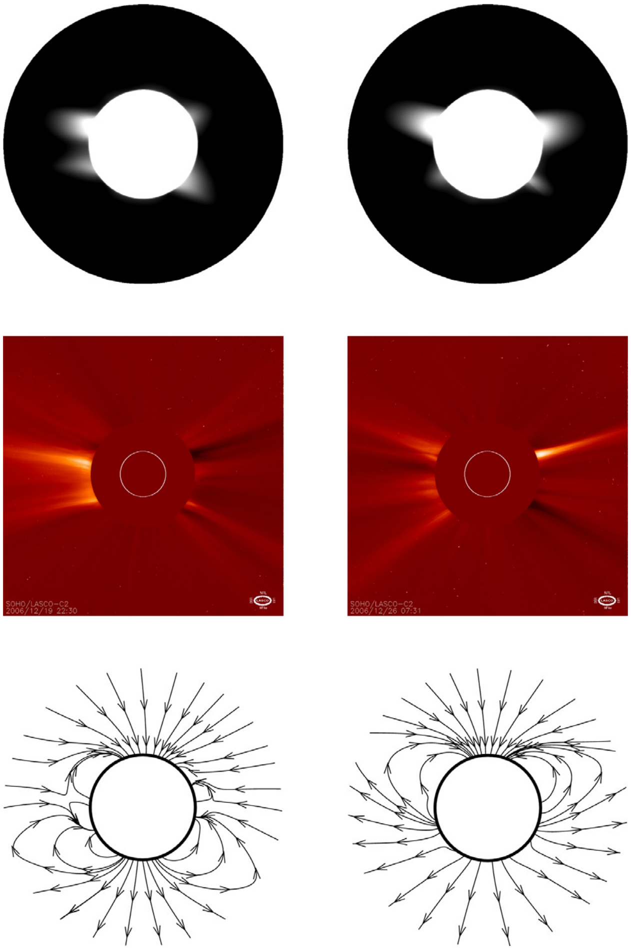

Fig. 4. The pB images from 2.3 to 6 R_s synthesized from the simulation at the meridian planes of $\phi = 180^\circ - 0^\circ$ (the top left panel) and $\phi = 270^\circ - 90^\circ$ (the top right panel) and observed on December 19, (the middle left panel) and 26 (the middle right panel), 2006 from SOHO/LASCO-C2, and the simulated magnetic field topologies from 1.0 to 2.6 R_s (the bottom panels) on the same meridional planes as in Row 1.

with

$$\mathcal{D}_{ii} = \Omega_i\left[\frac{\mathbf{I}}{\Delta t} - \frac{\partial \mathbf{S}_{\text{powell}}(\mathbf{U}_i, (\nabla \cdot \mathbf{B_1})_i)}{\partial \mathbf{U}_i} - \frac{\partial \mathbf{Q}_{\text{solar}}(\mathbf{U}_i)}{\partial \mathbf{U}_i}\right] - \frac{\partial \mathcal{F}_x(\mathbf{U}_i, \mathbf{U}_j)}{\partial \mathbf{U}_i},$$

$$\mathcal{L}_{ij} = -\frac{\partial \mathcal{F}_x(\mathbf{U}_i, \mathbf{U}_j)}{\partial \mathbf{U}_j} \qquad j < i,$$

$$\mathcal{U}_{ij} = -\frac{\partial \mathcal{F}_x(\mathbf{U}_i, \mathbf{U}_j)}{\partial \mathbf{U}_j} \qquad j > i.$$

The equations are approximately factored by neglecting the last term on the right-hand side of Eq. (12), and can be solved in the two steps that only involving simple block matrix inversions:

- Lower (forward) sweep:

  $(\mathcal{D} + \mathcal{L})\Delta\mathbf{U}^* = \mathbf{R}.$

- Upper (backward) sweep:

  $(\mathcal{D} + \mathcal{U})\Delta\mathbf{U} = \mathcal{D}\Delta\mathbf{U}^*.$

Finally the system can be solved by:

$$\Delta\mathbf{U}_i^* = \mathcal{D}^{-1}\left\{\mathbf{R} - \sum_{j:j<i}\frac{1}{2}\mathcal{R}^{-1}(\mathbf{n}_{ij})\left[\frac{\partial \mathbf{F}_x\Big(\mathcal{R}(\mathbf{n}_{ij})\mathbf{U}_{jR}\Big)\partial \mathbf{U}_j}{-}|\lambda_{ij}|\mathbf{I}\right]A_{ij}\Delta\mathbf{U}_j^*\right\},$$

$$\Delta\mathbf{U}_i = \Delta\mathbf{U}_i^* - \mathcal{D}^{-1}\left\{\sum_{j:j>i}\frac{1}{2}\mathcal{R}^{-1}(\mathbf{n}_{ij})\left[\frac{\partial \mathbf{F}_x\Big(\mathcal{R}(\mathbf{n}_{ij})\mathbf{U}_{jR}\Big)\partial \mathbf{U}_j}{-}|\lambda_{ij}|\mathbf{I}\right]A_{ij}\Delta\mathbf{U}_j\right\}.$$

4.2. GMRES algorithm

GMRES algorithm is the generalization of the conjugate gradient method proposed by Saad and Schultz [20] for solving a linear system where the coefficient matrix is not symmetric or positive definite. GMRES minimizes the norm of the computed residual vector over the subspace spanned by a certain number of orthogonal search directions, and the convergence speed of the iterative algorithm depends on the condition number of the coefficient matrix. So the preconditioner that attempts to cluster the eigenvalues at a single value is the easiest and most common way to improve the efficiency and robustness of GMRES [4]. GMRES with a LU-SGS preconditioner for Navier-Stokes equations developed by Luo et al. [4] not only converges effectively but also requires no additional memory storage by using the Jacobian matrix of the linearized scheme as a preconditioner matrix. By preconditioning Eq. (9) on the left, we have

$$\mathbf{P}^{-1}\mathbf{A}\Delta\mathbf{U} = \mathbf{P}^{-1}\mathbf{R},$$

with the LU-SGS preconditioner defined by $\mathbf{P} = (\mathcal{D} + \mathcal{L})\mathcal{D}^{-1}(\mathcal{D} + \mathcal{U})$. The preconditioned restarted GMRES(m) is described as Algorithm 1.

5. Numerical results

To validate the capability of the scheme proposed above, we employ it to numerically study the ambient solar wind of CR 2051, which lasted from December 12, in 2006 to January 7, in 2007 in the descending phase during the solar minimum. The computational domain of the solar wind evolution ranges from the solar surface to 20 R_S. In the computational domain, the time-independent $\mathbf{B_0}$ is a 3D global magnetic field produced by utilizing the potential field (PF) model based on the radial photospheric magnetic data from the Global Oscillation Network Group

Algorithm 1 GMRES with LU-SGS preconditioner.

```
Input: $\triangle \mathbf{U}_0, \mathbf{A}, \mathbf{R}, \mathbf{P}$
Output: $\triangle \mathbf{U}_0$
$L2_{last} = +\infty$
for itr=1, itr$_{\max}$ do¡¡¡¡
    $\mathbf{v}_0 := \mathbf{R} - \mathbf{A}\triangle \mathbf{U}_0$
    $\mathbf{r}_0 := \mathbf{P}^{-1}\mathbf{v}_0$                LU-SGS as the preconditioner
    ExchangeBoundary($\mathbf{r}_0$)            Through the six-component grid system
    $\beta := \|\mathbf{r}_0\|_2$                    Initial residual norm
    $\mathbf{v}_1 := \mathbf{r}_0/\beta$
    for j=1, m do                      GMRES(m)¡¡¡¡
        $\mathbf{v}_0 := \mathbf{A}\mathbf{v}_j$
        $\mathbf{v}_{j+1} := \mathbf{P}^{-1}\mathbf{v}_0$          LU-SGS as the preconditioner
        ExchangeBoundary($\mathbf{v}_{j+1}$)    Through the six-component grid system
        for i=1, j do                  Gram-Schmidt step
            $h_{i,j} := (\mathbf{v}_{j+1}, \mathbf{v}_i)$
            $\mathbf{v}_{j+1} := \mathbf{v}_{j+1} - h_{i,j}\mathbf{v}_i$
        $h_{j+1,j} := \|\mathbf{v}_{j+1}\|_2$
        $\mathbf{v}_{j+1} := \mathbf{v}_{j+1}/h_{j+1,j}$
    $\mathbf{z} := \min_{\hat{\mathbf{z}}} \|\beta\mathbf{e_1} - H\hat{\mathbf{z}}\|_2$
    $\Delta\mathbf{U}_0 := \Delta\mathbf{U}_0 + \sum_{i=1}^{m} \mathbf{v}_i\mathbf{z}$
    $L2 = \|\beta\mathbf{e_1} - H\mathbf{z}\|_2$¡¡¡¡
    if $L2 < \epsilon$ or $L2 > L2_{last}$ then exit          Stopping Criterion
    $L2_{last} = L2$
return $\triangle \mathbf{U}_0$
```

(GONG) program, and the time-dependent magnetic field $\mathbf{B_1}$ is initially set as zero. The initial distributions of plasma mass density ρ, pressure p and velocity $\mathbf{v}$ are given by Parker's solar wind flow [21]. The temperature and number density on the solar surface are $T_S = 1.3 \times 10^6$K and $\rho_S = 1.5 \times 10^8 \mathrm{cm}^{-3}$, respectively.

We take the L_2 norm of the residual as a criterion to check convergence, and the solution tolerance ϵ is set to 1.0×10^{-4}. The maximum allowable number of iterations $itr_{\max}$ is set to 20. However, this criteria is often not reached within the allowable number of iterations. We found in practice that, the L_2 norm of the residual declines during the first several iterations, and then it hovers around some extent. For the purpose of not wasting efforts and time in extra iterations, we set another stopping criterion for iterations, i.e. when the L_2 norm of the residual is larger than that in the last iteration.

Our computing environment is offered by TH-1A supercomputer from National Supercomputing Center in TianJin, China. Each node on TH-1A is equipped with two Intel Xeon X5670@2.93GHz high-performance processors. Every program employs 120 processes and runs on 10 nodes parallelly by utilizing message passing interface (MPI) for communication. In this section, time cost and memory storage for the implicit and explicit scheme are compared, and then the simulated results of steady solar wind for CR 2051 are presented and compared with observational ones. It should be noticed here that, in the following we present the simulated pictures from the implicit scheme by default, unless otherwise specified.

5.1. Time cost and memory storage

To testify the efficiency of our implicit solver, we make a comparison between the implicit and explicit solvers that adopt the same FV scheme. As the simulation of the ambient solar wind is a steady problem, we measure the time cost of reaching a basically steady state, of which the termination criterion of the simulation is set as $\left|\frac{\rho^{n+1}-\rho^n}{\rho^n}\right| \le 3.9 \times 10^{-7}$. As usual, the CFL number in the explicit solver is set as 0.5, while the CFL number is enlarged to 100 in the implicit solver. Table 1 presents the time spent for two sampled mesh divisions, i.e. $115 \times 42 \times 42$ and $150 \times 62 \times 62$ meshes in (r, θ, ϕ) per component. The averages of the time costs are used for comparison after each program runs 5 times. With the mesh division of $115 \times 42 \times 42$, the explicit solver takes 33.77 h of wall time, while the implicit solver costs only about 1.08 hours, with a speedup ratio of $31.27\times$. As for the mesh division of $156 \times 62 \times 62$ in (r, θ, ϕ), the implicit solver only takes an average of 3.29 hours of wall time, which is 28.05x times faster than the explicit one. The speedup ratio of the $156 \times 62 \times 62$ mesh division is somewhat smaller than that of the $115 \times 42 \times 42$ mesh division. This is because that with more meshes, the implicit solver costs nonlinearly more calculation and time to converge a steady state. Even so, the speedup with denser mesh is very impressive, by reducing the time cost from several days to only a few hours.

Table 1
Time costs of the implicit and the explicit solvers.

Cell number per component	Implicit (h)	Explicit (h)	time ratio (x)
$115 \times 42 \times 42$	1.08	33.77	31.27
$156 \times 62 \times 62$	3.29	92.30	28.05

The utilization of the GMRES with an LU-SGS preconditioner in the implicit solver not only significantly speeds up the convergence, but releases us from storing the large matrix of the equation system, which is also crucial to large-scale studies. Especially in our parallel and distributed computation, it is almost impracticable. By using the Jacobian matrix of the linearized scheme as the preconditioner matrix, LU-SGS preconditioner can be directly derived from the available flux term without storing the large matrix of the equations.

5.2. Comparisons between the modeled and observational results

In this part, we make comparisons of the simulated results with the available coronal observations and mapped interplanetary measurements from different perspectives, such as coronal holes,

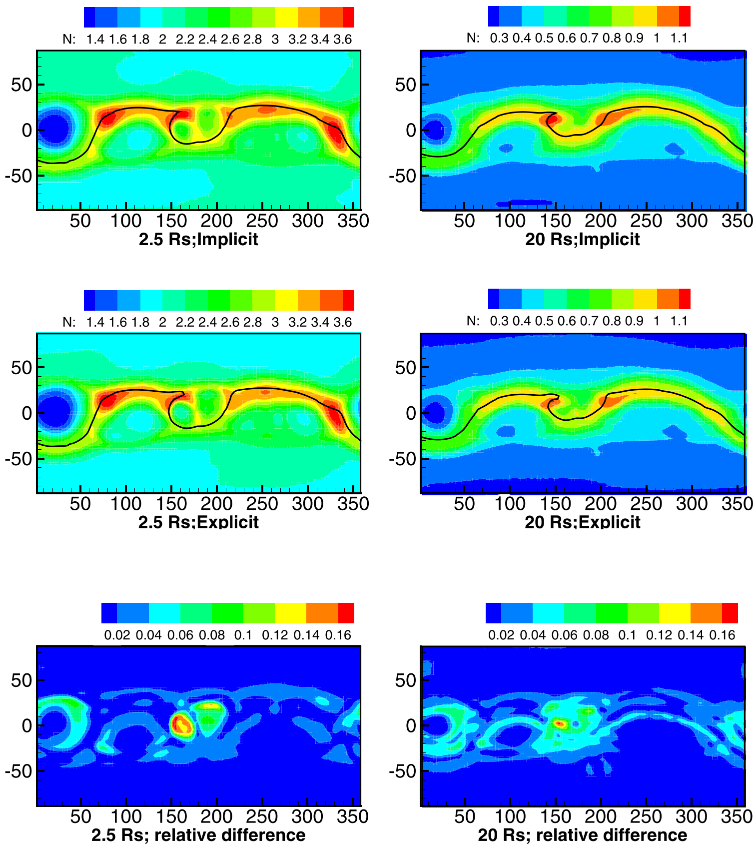

Fig. 5. Longitude-latitude maps of the proton number density at 2.5 R_s with unit of $10^5 cm^{-3}$ (the left column) and at 20 R_s with unit of $10^3 cm^{-3}$ (the right column). The first and the second rows are maps simulated by the implicit and the explicit solvers, respectively. The black lines in these maps denote the magnetic neutral lines. The third row is maps of the relative difference between the proton number densities modeled from the implicit and the explicit solvers.

bipolar and unipolar coronal streamers, the HCS and high- and low-speed streams.

Solar coronal holes where the magnetic field lines extend to the heliosphere are the most easily-recognized signatures that appear as dark regions in X-ray and EUV images due to reduced emission from solar plasma localized at open magnetic field footpoints [22–25]. Fig. 3 displays the longitude-latitude maps of the coronal holes near the solar surface simulated by the MHD model (left) and observed by the 195 Åobservations (right) from the Extreme ultraviolet Imaging Telescope (EIT) on board the SOlar and Heliospheric Observatory (SOHO). In the left panel, open-field regions are shaded black while the closed-field regions white. The open- and closed-field regions are determined by tracing the magnetic field lines from 6 R_s back to the photosphere. As for the observed map, coronal holes are represented by dark color. From both maps, we can find that the equatorward boundaries of both polar coronal holes (PCHs) in the simulation almost coincide the observation. What is more, the shapes and locations of the extending holes from the southern PCH are well captured by the model. It is also characterized for the observation of CR 2051 that a band-shaped isolated coronal hole appears in low-latitude region at the Longitude of around 100°, which is reproduced in the simulated map as well. De Toma [26] and Yang [27] discovered that a significant portion of the solar surface was covered with the middle- and low-latitude coronal holes in the 2006–2009 solar minimum, and point out that their presence resulted from the relatively weak polar magnetic fields in this solar minimum.

Corresponding to the pattern of open- and closed-field regions near the solar surface, the coronal plasma exhibits non-uniform distribution that can well be qualitatively represented by the coronal white-light polarized brightness (pB) images produced by Thomson scattering from free electrons in the coronal plasma [28–30]. In Fig. 4, we compare the numerical results and the observational at the meridian planes to demonstrate that our solver can achieve the synthesized coronal white-light pB images basically consistent with the observation. The first row are the pB images synthesized from the simulated result from 2.3 to 6 R_s at the planes of $\phi = 180^\circ - 0^\circ$ (left column) and $\phi = 270^\circ - 90^\circ$ (right column) and the second row are those observed by the Large Angle and Spectrometric Coronagraph C2 (LASCO-C2) onboard SOHO with the same radius range as before. The left coronal picture is taken at the seventh day of the CR, corresponding to the observation at the $\phi = 180^\circ - 0^\circ$ plane while the right one is taken at the fourteenth day, corresponding to the numerical $\phi = 270^\circ - 90^\circ$ plane. Both these observational and numerical pictures show streamers ranging from 2.3 to 6 R_s. From the modeled and observed pB images, we observe that the streamer-like structures do not extend radially outward from their foot points, but cover relatively larger latitudes near the Sun [27]. Furthermore, we can find that two broad bright structures extend outward at the east limb and a few diffusive bright structures covers the west limb for the pB image on the plane of $\phi = 180^\circ - 0^\circ$. For the observed and synthesized pB images of the meridian plane of $\phi = 270^\circ - 90^\circ$, two bright structures are captured at the east limb and one brightest and sharpest structure is reproduced at the latitude of 30°N at the west limb. Comparing the pB images with the modeled magnetic field topologies in the third row, we can easily deduce that northeast structure at the plane of $\phi = 180^\circ - 0^\circ$ corresponds to the emission from the unipolar streamer at the latitude of 25 °N and the other bright structures result from bipolar streamers. It should be

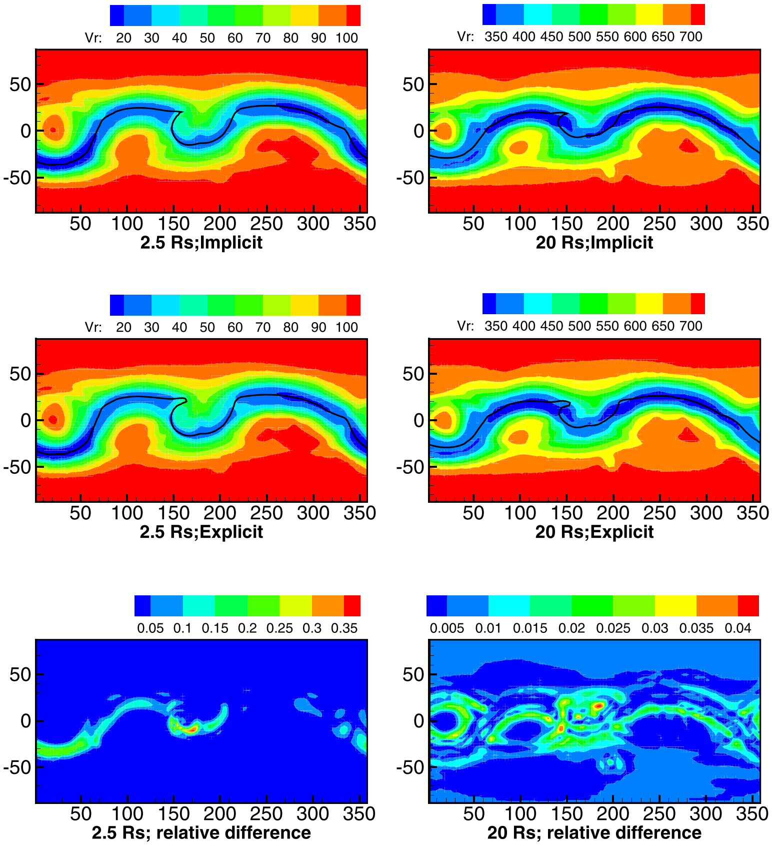

Fig. 6. Longitude-latitude maps of the radial speed at 2.5 R_s (the left column) and at 20 R_s (the right column) with unit of km s^{-1}. The first and the second rows are maps simulated by the implicit and the explicit solvers, respectively. The black lines in these maps denote the magnetic neutral lines. The third row is maps of the relative difference between the radial speeds modeled from the implicit and the explicit solvers.

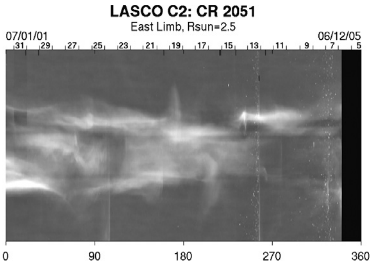

Fig. 7. The synoptic map of the white-light polarized brightness at the east limb from SOHO/LASCO-C2.

noted that the faint structure at the northwest limb of the plane of $\phi = 180^\circ - 0^\circ$ comes from the low emission from an isolated coronal hole, which can be inferred from Figs. 5 and 6.

It is instructive to validate the capability of the model developed in the previous sections by comparing the simulated results from the proposed implicit and explicit solvers. In Fig. 5, we present longitude-latitude maps for the proton number density from the implicit solver (top panels) and the explicit one (middle panels) and the relative difference between them at 2.5 R_s (bottom left panel) and 20 R_s (bottom right panel). The corresponding maps for the radial velocity of plasma flows are displayed in Fig. 6. Here the relative differences of the proton density and the radial velocity are defined as $\left|\frac{\rho_{\mathrm{im}}-\rho_{\mathrm{ex}}}{\rho_{\mathrm{im}}}\right|$ and $\left|\frac{V_{\mathrm{rim}}-V_{\mathrm{rex}}}{V_{\mathrm{rim}}}\right|$, respectively, with subscripts “im” and “ex” referring to the implicit and the explicit solvers. The black line in each panel of the top and middle rows denotes the magnetic neutral line (MNL), the extension of which shapes the HCS. The HCS is one of the most important interplanetary structures because it separates oppositely directed magnetic field lines, and various solar wind parameters vary with the distance from the HCS. From Figs. 5 and 6, the simulated results from both the implicit and the explicit solvers show that the coronal plasma moves faster at a larger heliocentric distance. Both figures also reveal that the HCS can be described as a two-hump and two-trough wavy structure, and the high-density low-speed plasma flow dominates the area in the vicinity of the HCS. Meanwhile, the low-density and high-speed plasma flow pervades the polar or high-latitude regions. Additionally, we find that there are very small relative differences between the densities and between the radial speeds achieved from the implicit and the explicit solvers. For most regions, the relative differences between the modeled densities are below 0.04 and the relative differences between the modeled radial speeds are less than 0.05.

The white-light polarized brightness at the east limb from SOHO/LASCO C2 at 2.5 R_s for CR 2051 are presented in Fig. 7. By comparing the longitude-latitude map at 2.5 R_s with the synoptic map of pB observation, we find that the area near the magnetic neutral is characteristic of the bright structures. Roughly speaking, the HCS at 20 R_s is similar to the magnetic neutreal line at 2.5 R_s, while the magnetic neutral line at 2.5 R_s extends a little higher latitude than the HCS at 20 R_s. There are subtle differences between them by examining carefully. In addition, the first rising slope and the last falling gradient at 20 R_s become more gentle than those at 2.5 R_s.

Fig. 8 shows the magnetic filed lines at the meridian plane of $\phi = 180^\circ - 0^\circ$ (top row) and $\phi = 270^\circ - 90^\circ$ (bottom row). The radial speed Vr on the left column and the number density N on

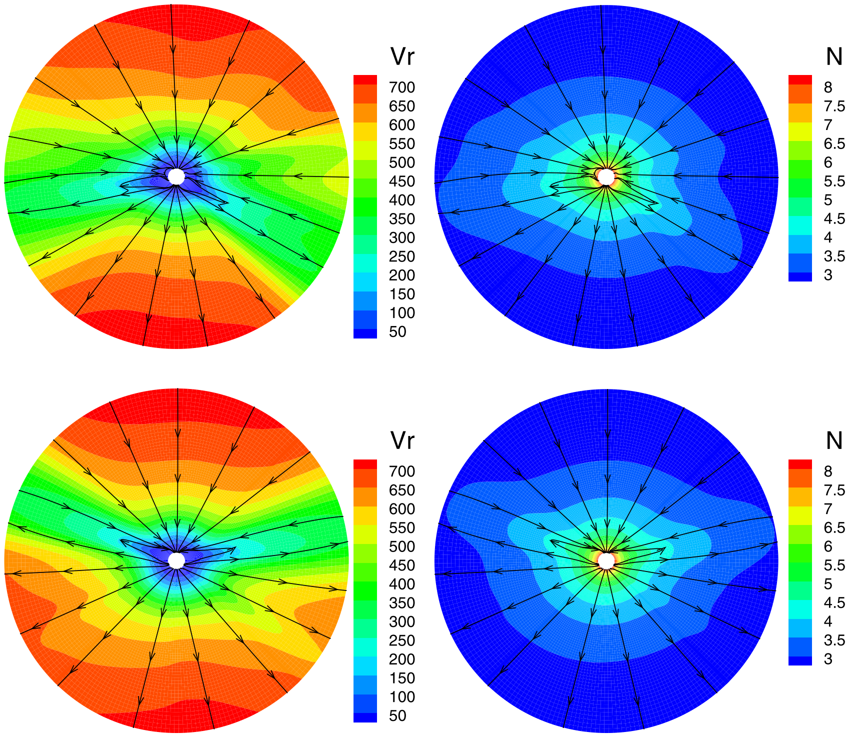

Fig. 8. Magnetic filed lines on the meridian plane of $\phi = 180^\circ - 0^\circ$ (top panels) and $270^\circ - 90^\circ$ (bottom panels) with the superposed radial bulk speed (unit: km s^{-1}) (left panels) and the logarithm of the proton number density (unit: cm^{-3}) to base 10 (right panels) in color contours.

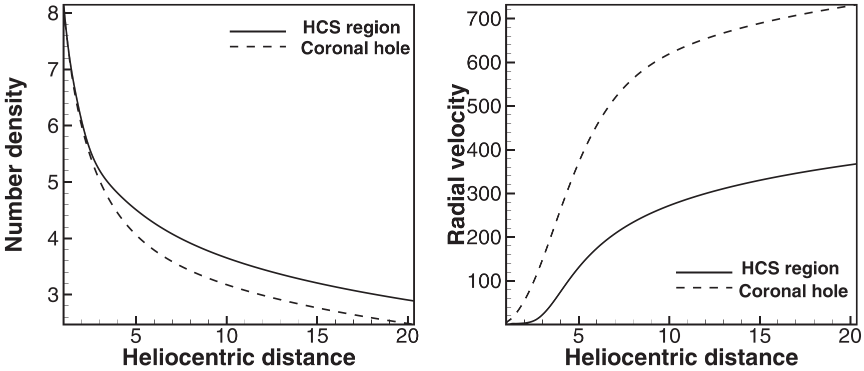

Fig. 9. Radial profiles of the logarithm of the proton number density (unit: cm^{-3}) to base 10 (left) and the radial bulk speed with unit of km s^{-1} (right). The solid line denotes the profiles in the HCS region with $(\theta, \phi) = (-29^\circ, 1^\circ)$, and the dashed line denotes the profiles in the coronal hole with $(\theta, \phi) = (5^\circ, 8^\circ)$.

the right column are also superposed in color contours, while the arrowheads on the black lines represent the directions of the magnetic fields. The figure shows the same pattern of the high- and low-speed solar wind as Fig. 6 and a helmet streamer stretched by the solar wind. Between different magnetic polarities forms a thin current sheet.

To further demonstrate the radial variations of the solar wind parameters in coronal holes and near the HCS region, we shows the number density and radial velocity profiles along two radial lines ranging from 1 R_s to 20 R_s in Fig. 9. The solid lines represent the profiles in the HCS region along the radial line of $(\theta, \phi) = (-29^\circ, 1^\circ)$, while the dashed lines denote the profiles in the coronal hole along the radial line of $(\theta, \phi) = (5^\circ, 8^\circ)$. The proton number densities in the HCS region and in coronal hole are almost the same near the solar surface. With the heliocentric distance increasing from 1 R_s to 20 R_s, the density in the HCS region keeps higher than that in coronal hole, and the gap between them becomes more significant. What's more, this trend will maintain in interplanetary space. The figure demonstrates that the solar wind speed rises from about 340 km s^{-1} at 5 R_s to about 720 km s^{-1} at 20 R_s, which is compatible with the previous study on coronal observations [31]. Meanwhile, the solar wind speed near the MNL increases from about 140 km s^{-1} to about 360 km s^{-1}, which agrees with the conclusion inferred from time-lapse sequences of white-light images [32].

In order to fill the observational gap near the outer boundary in our simulation, we map the in-situ measurements at 1 AU back to 20 R_s by using a ballistic approximation [e.g., 27], which assumes a plasma parcel travels from 20 R_s to the spacecraft with at a speed measured at 1 AU. The temporal profiles of the radial solar wind speed and the radial magnetic field polarities at 20 R_s are shown in Fig. 10 with the simulated results denoted by red lines and the mapped observational results of the OMNI data by black lines. We can easily find that the profiles of the solar wind from both the simulation and the in-situ observation go with the same trend in general. In the profile of the radial velocity, it is characterized of

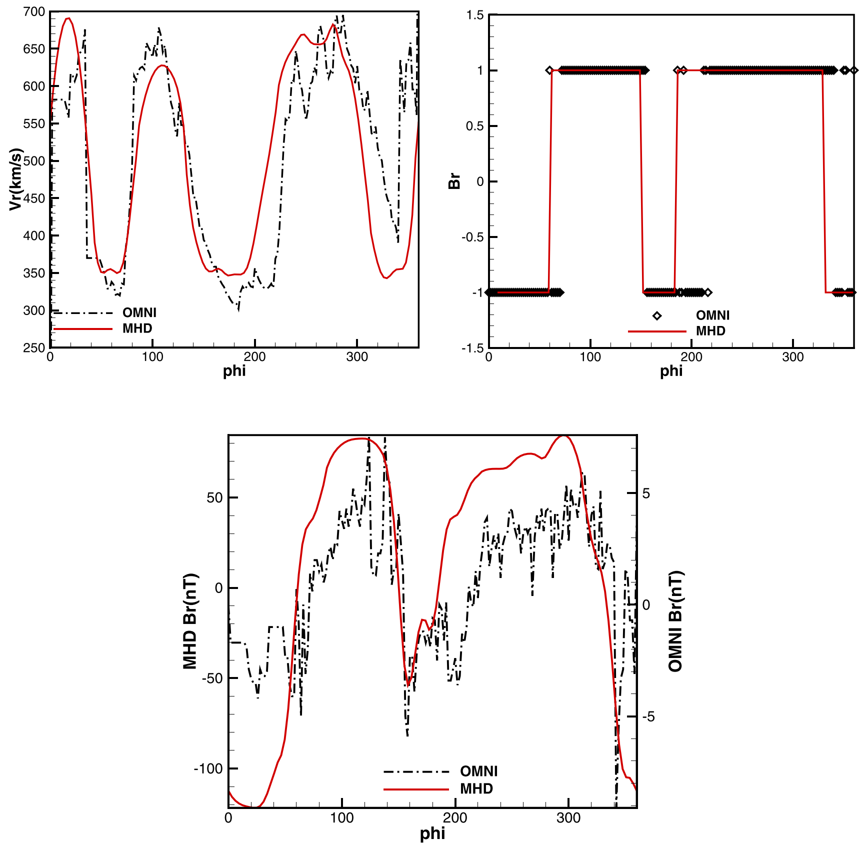

Fig. 10. The simulation (red) and the mapped measurements of the OMNI data (black) at 20 R_s are present with Carrington longitudes. The top panel shows the variation of the radial speeds (left) with unit of km s^{-1}, and the magnetic field polarities (right), where “1” stands for the radial magnetic field away from the Sun and “-1” towards the Sun. The bottom panel is the variations of the intensities of the radial magnetic fields with unit of nT. (For interpretation of the references to colour in this figure legend, the reader is referred to the web version of this article.)

three high-speed peaks centered at Longitudes 25°, 100° and 260° and three low-speed streams centered at Longitudes 60°, 180° and 340° in the OMNI data. All of these streamers are captured at precisely same longitudes by the simulated result. As for the speed maxima, the high-speed peaks in simulation range between 640 km s^{-1} and 680 km s^{-1}, while the low-speed streams flows at a speed of 350 km s^{-1}. We also note that the speed of the simulated stream at Longitude 100° is a little lower than the OMNI data. The polarities of the radial magnetic field is on the right of the top panel in Fig. 10. Though there are a few deviations, sectors of different polarity of the numerical result are generally in agreement with that of the observation. The hit ratio of the simulated radial magnetic field polarities to the observed ones for CR 2051 is 84.53%. This possibly results from both the error of the simulated results and the effect of the waves and perturbations in the solar wind that can lead to the opposite polarity to be measured rather than the true field polarity [27,33]. To sum up, high- and low-speed streams are captured by our MHD model, and the observed polarities of the radial magnetic field are mostly reproduced by our simulation with reasonable accuracy. In the bottom panel of Fig. 10, we also present the longitudinal variations of the radial magnetic fields at 20 R_S achieved from the simulation and the mapped in-situ measurements without considering the factor of r^{-2}. If we take this factor into account, the modeled radial magnetic fields are only one-third of the corresponding measurements, which is also present in previous studies [34–37]. Linker [37] attributed the deficiency of the open magnetic flux to either the underestimation of the Sun’s magnetic flux by typical observatory maps, or other sources of open magnetic flux other than the regions that are obviously dark in EUV and X-ray emission.

6. Conclusions

In this paper, we develop an easily implemented FV scheme with the GMRES algorithm and an LU-SGS preconditioner on the six-component mesh grid system to solve the MHD equations governing the solar wind plasma. The implicit and the explicit solvers of the same FV scheme are implemented and run on the same computing cluster by evoking 120 processes. The comparisons show that the implicit solver can effectively shorten the time cost from several days to only a few hours and aquire speedup ratios of 31.27 × and 28.05 ×, with two sampled mesh divisions. Besides the significant computational efficiency, the LU-SGS preconditioner does not require any additional memory storage and is easy to implement on the parallelly distributed cluster. We further employ the proposed MHD scheme to simulate the 3D large-scale structures of the steady-state solar wind from 1 R_S to 20 R_S during CR 2051. The simulated results capture many features of the solar corona. The simulation and the observation achieve similar isolated low-latitude coronal holes and almost the same shapes and sizes of the PCHs. The white-light pB images synthesized from the simulated results and observed by LASCO/SOHO show basically consistent distributions of bright structures. In addition, the radial profiles of the solar wind radial bulk speed from 2.6 R_S to 20 R_S are consistent with previous observational studies [31,32]. The simulated results at 20 R_S capture the mapped in-situ observations with reasonable accuracy. Therefore the simulation exhibits the potential capability of numerically modeling the space weather event from the Sun to interplanetary space.

Generally speaking, it is formidable to conduct the real-time 3D MHD simulation for a specified space weather events from the Sun to the Earth beyond because the simulation is too time-consuming and needs too much computational resources. The significant computational efficiency of the FV scheme with a GMRES algorithm and an LU-SGS preconditioner will be a promising choice to complete the tough task after improvements, which will be our future consideration in further studies http://omniweb.gsfc.nasa.gov.

Acknowledgments

The work is jointly supported by the National Natural Science Foundation of China (Grant Nos. 41531073, 41231068, 41731067, 41574171, and 41504132) and the Specialized Research Fund for State Key Laboratories. This work utilizes data obtained by the Global Oscillation Network Group (GONG) program, managed by the National Solar Observatory, which is operated by AURA, Inc. under a cooperative agreement with the National Science Foundation. The SOHO/LASCO data used here are produced by a consortium of the Naval Research Laboratory (USA), Max-Planck-Institut fuer Aeronomie (Germany), Laboratoire d'Astronomie (France), and the University of Birmingham (UK). The OMNI data are obtained from the GSFC/SPDF OMNIWeb interface at http://omniweb.gsfc.nasa.gov. The computing environments of this work are offered by TH-1A supercomputer from National Supercomputing Center in Tianjin, China. The authors are appreciated for our reviewers' constructive suggestions for the improvement of the manuscript.

References

[1] Feng X, Zhang M, Zhou Y. A new three-dimensional solar wind model in spherical coordinates with a six-component grid. Astrophys J Suppl Ser 2014;214(1):6. doi:10.1088/0067-0049/214/1/6.

[2] Jardin SC. Review of implicit methods for the magnetohydrodynamic description of magnetically confined plasmas. J Comput Phys 2012;231(3):822–38.

[3] Jones OS, Shumlak U, Eberhardt DS. An implicit scheme for nonideal magnetohydrodynamics. J Comput Phys 1997;130(2):231–42.

[4] Luo H, Baum JD, Löhner R. A fast, matrix-free implicit method for compressible flows on unstructured grids. J Comput Phys 1998;146(2):664–90.

[5] Jameson A, Yoon S. Lower-upper implicit schemes with multiple grids for the euler equations. AIAA J 1987;25(7):929–35.

[6] Sitaraman H, Raja LL. A matrix free implicit scheme for solution of resistive magneto-hydrodynamics equations on unstructured grids. J Comput Phys 2013;251:364–82.

[7] Feng X, Yang L, Xiang C, Wu ST, Zhou Y, Zhong D. Three-dimensional solar wind modeling from the sun to earth by a SIP-CESE MHD model with a six–component grid. Astrophys J 2010;723(1):300.

[8] Ogino T, Walker RJ. A magnetohydrodynamic simulation of the bifurcation of tail lobes during intervals with a northward interplanetary magnetic field. Geophys Res Lett 1984;11(10):1018–21.

[9] Tanaka T. Finite volume TVD scheme on an unstructured grid system for three--dimensional MHD simulation of inhomogeneous systems including strong background potential fields. J Comput Phys 1994;111(2):381–9.

[10] Toth GZ. The $\nabla \cdot \mathbf{B} = 0$ constraint in shock-capturing magnetohydrodynamics codes. J Comput Phys 2000;161(2):605–52.

[11] Powell KG, Roe PL, Linde TJ, Gombosi TI, De Zeeuw DL. A solution-adaptive upwind scheme for ideal magnetohydrodynamics. J Comput Phys 1999;154(2):284–309.

[12] Nakamizo A, Tanaka T, Kubo Y, Kamei S, Shimazu H, Shinagawa H. Development of the 3-D MHD model of the solar corona-solar wind combining system. J Geophys Res 2009;114(A7).

[13] Tanaka T. Configurations of the solar wind flow and magnetic field around the planets with no magnetic field: calculation by a new MHD simulation scheme. J Geophys Res 1993;98(A10):17251. doi:10.1029/93ja01516.

[14] Dedner A, Kemm F, Krner D, Munz CD, Schnitzer T, Wesenberg M. Hyperbolic divergence cleaning for the MHD equations. J Comput Phys 2002;175(2):645–73. doi:10.1006/jcph.2001.6961.

[15] Yalim MS, Vanden Abeele D, Lani A, Quintino T, Deconinck H. A finite volume implicit time integration method for solving the equations of ideal magnetohydrodynamics for the hyperbolic divergence cleaning approach. J Comput Phys 2011;230(15):6136–54. doi:10.1016/j.jcp.2011.04.020.

[16] Ivan L, De Sterck H, Northrup SA, Groth CPT. Multi-dimensional finite-volume scheme for hyperbolic conservation laws on three-dimensional solution-adaptive cubed-sphere grids. J Comput Phys 2013;255:205–27. doi:10.1016/j.jcp.2013.08.008.

[17] Venkatakrishnan V. On the accuracy of limiters and convergence to steady state solutions. Tech. Rep.. AIAAPaper93 0880; 1993.

[18] Barth T.J.. Analysis of implicit local linearization techniques for upwind and TVD algorithms, 1987. AIAA Paper 87–0595.

[19] Nejat A, Ollivier-Gooch C. A high-order accurate unstructured Newton-Krylov solver for inviscid compressible flows, AIAA 2006–3711. Fluid dynamics and co-located conferences. San Francisco, California: American Institute of Aeronautics and Astronautics; 2006. doi:10.2514/6.2006-371110.2514/6.2006-3711.

[20] Saad Y, Schultz MH. Gmres: a generalized minimal residual algorithm for solving nonsymmetric linear systems. Siam J Sci Stat Comput 1986;7(3):856–69.

[21] Parker EN, Marshak RE, Johnson GW. Interplanetary dynamical processes. Phys Today 1964;17(3). 72–72

[22] Cranmer SR. Coronal holes. Living Rev Sol Phys 2009;6:3. doi:10.12942/lrsp-2009-3.

[23] de Toma G. Evolution of coronal holes and implications for high-speed solar wind during the minimum between cycles 23 and 24. solphys 2011;274(1):195–217.

[24] Wang YM. Small coronal holes near active regions as sources of slow solar wind. apj 2017;841:94. doi:10.3847/1538-4357/aa706e.

[25] Lowder C, Qiu J, Leamon R. Coronal holes and open magnetic flux over cycles 23 and 24. solphys 2017;292:18. 1612.07595

[26] De Toma G. Evolution of coronal holes and implications for high-speed solar wind during the minimum between cycles 23 and 24. Sol Phys 2011;274(1):195–217.

[27] Yang LP, Feng XS, Xiang CQ, Liu Y, Zhao X, Wu ST. Time-dependent MHD modeling of the global solar corona for year 2007: driven by daily-updated magnetic field synoptic data. J Geophys Res (Space Physics) 2012;117:A08110.

[28] Billings DE. A guide to the solar corona. New York: Academic; 1966.

[29] Linker JA, Mikić Z, Biesecker DA, Forsyth RJ, Gibson SE, Lazarus AJ, Lecinski A, Riley P, Szabo A, Thompson BJ. Magnetohydrodynamic modeling of the solar corona during whole sun month. J Geophys Res 1999;104:9809–30.

[30] Hayes AP, Vourlidas A, Howard RA. Deriving the electron density of the solar corona from the inversion of total brightness measurements. APJ 2001;548:1081–6.

[31] Pätzold M, Tsurutani BT, Bird MK. An estimate of large-scale solar wind density and velocity profiles in a coronal hole and the coronal streamer belt. J Geophys Res 1997;102(A11):24151–60. doi:10.1029/97JA01868.

[32] Sheeley NR Jr, Wang YM, Hawley SH, Brueckner GE, Dere KP, Howard RA, Koomen MJ, Korendyke CM, Michels DJ, Paswaters SE, Socker DG, Cyr OCS, Wang D, Lamy PL, Llebaria A, Schwenn R, Simnett GM, Plunkett S, Biesecker DA. Measurements of flow speeds in the corona between 2 and 30 R_s. APJ 1997;484(1):472.

[33] Lepri ST, Antiochos SK, Riley P, Zhao L, Zurbuchen TH. Comparison of heliospheric in situ data with the quasi-steady solar wind models. Astrophys J 2008;674(2):1158–66.

[34] Riley P. An alternative interpretation of the relationship between the inferred open solar flux and the interplanetary magnetic field. Astrophys J Lett 2007;667:L97–L100. doi:10.1086/522001.

[35] Khabarova O, Obridko V. Puzzles of the interplanetary magnetic field in the inner heliosphere. Astrophys J 2012;761:82. doi:10.1088/0004-637X/761/2/82. 1204.6672

[36] Feng X, Ma X, Xiang C. Data-driven modeling of the solar wind from 1 r_s to 1 AU. J Geophys Res 2015;120:10. doi:10.1002/2015JA021911.

[37] Linker JA, Caplan RM, Downs C, Riley P, Mikic Z, Lionello R, Henney CJ, Arge CN, Liu Y, Derosa ML, Yeates A, Owens MJ. The open flux problem. Astrophys J 2017;848:70. doi:10.3847/1538-4357/aa8a70. 1708.02342